Pose Estimation of UAVs Based on INS Aided by Two Independent Low-Cost GNSS Receivers

Martin L. Sollie[1], Torleiv H. Bryne[1] and Tor Arne Johansen[1]

Abstract— **Increasing use of UAVs in high-precision applications, such as georeferencing and photogrammetry, increases the requirements on the accuracy of the estimated position, velocity and attitude of the vehicle. Commercial systems that utilize magnetometers in the heading estimates are cheap, but are affected by disturbances from both the vehicle itself, nearby metal structures and variations in the Earth's magnetic field. On the other side, commercial dual-antenna satellite navigation systems can provide the required accuracy, but are expensive. This paper explores the use of a low-cost setup using two independent GNSS receivers, aiding an inertial navigation system by using pseudorange, Doppler frequency and carrier phase measurements from two longitudinally separated receivers on a fixed-wing UAV. The sensor integration was based on a multiplicative extended Kalman filter (MEKF). The main contribution of this paper is the derivation of measurement models for the raw GNSS measurements based on the MEKF error state, taking into account antenna lever arms and explicitly including the difference in measurement time between the receivers in the measurement model for double differenced carrier phase. The proposed method is verified using data collected from a UAV flight.**

I. Introduction

The small unmanned aerial vehicles (UAVs) used by hobbyists and professionals today are commonly equipped with an autopilot system estimating its position, velocity and attitude using one or more inertial measurement units (IMUs) containing gyros and accelerometers, a single global navigation satellite system (GNSS) receiver, a barometer and a magnetometer (magnetic compass). Examples of such systems are the Pixhawk series of flight controllers [1]. GNSSs provides position and velocity measurements which are free of long-term drift. However, there are many challenges with GNSS as a source of position and velocity information. The measurements are normally available at a rate too low for feedback control in highly dynamic systems, such as UAVs, and the measurements can be noisy. Because the signals received from the satellites have low power, the receivers can be disturbed by interference, jamming or spoofing. Obstructions between the receiver and satellites can block the signals, making it less suitable in valleys or dense urban environments and basically unsuitable for indoor navigation.

The use of an inertial navigation system (INS), consisting of an IMU and the processing required to estimate position, velocity and attitude, offers several advantages. As it is completely self contained and does not rely on any external signals, it is not exposed to external interference. The measurements also typically have low noise and are available at a high rate, giving smooth position and attitude outputs. The drawback of inertial navigation is that all IMUs experience slowly varying errors that cause position and attitude estimates, based on the mechanization of angular rate and specific force, to drift over time.

Due to the complementary nature of INS and GNSS, combining the measurements using an estimation algorithm such as the Kalman filter [2] can give the best of both worlds. The long-term drift is eliminated by estimating and compensating the INS errors using GNSS measurements, while the INS is used to smooth the output and provide position, velocity and attitude (PVA) estimates even when not receiving GNSS receiver measurement. The use of tightly coupled integration, where raw GNSS measurements are used directly, instead of intermediate calculation of GNSS-only state estimates, allows correction of the INS estimates even when only a few satellites are visible such that a complete GNSS position solution is not available.

UAVs using today's low cost autopilot systems are mostly used for waypoint flying and other tasks where small attitude errors pose no large problem as a deviation from the desired flight path, which is visible in the observed position and velocity errors, is handled using feedback control. For these uses having a correct course (direction of movement) is more important than a correct heading. Other applications however, such as georeferencing, photogrammetry and mapping, require more accurate state estimates. It is especially the accurate estimation of the vehicle heading which is a challenge [3]. For UAVs flying in a steady state, or hovering, with low acceleration and angular rate, the errors in attitude and IMU biases are not observable with only a single GNSS antenna, and the estimate will rely on the magnetic compass. Magnetometers are susceptible to disturbances from irregularities in the Earth's magnetic field, or ferrous materials or electrical currents close to the sensor [3]. They are also not very useful when navigating near the magnetic poles, and the local magnetic declination values for the areas of operation must be known. Improved estimates of heading can be obtainted by the use of dual-antenna GNSS, and with three or more antennas full attitude can also be determined. Commercial systems using GNSS for heading or attitude, such as the Vectornav VN-300 [4], are however significantly more expensive than the autopilot systems discussed.

This motivates the use of low-cost commercial-off-the-shelf receivers for aiding in estimation of heading or attitude. The determination of attitude using dedicated multi-antenna

This work was partially supported by the Norwegian Research Council, projects no. 223254, 282427 and 250725

[1]Department of Engineering Cybernetics, The Norwegian University of Science and Technology, Trondheim, Norway.

Corresponding author: martin.l.sollie@ntnu.no

receivers, where a single common clock is used for all tracking, has been researched by multiple authors [5]–[10]. The use of a common clock, which is not the case when multiple independent receivers are used, simplifies the measurement processing, but requires dedicated hardware. The use of non-dedicated receivers has two main properties that must be adressed:

1) Different receivers have different clock errors.
2) Measurements from the different receivers are not necessarily sampled at the same instant.

The second point is mainly a result of the first, as the receivers schedule raw measurement outputs according to their local clocks, but also occurs if the receivers schedule their measurements at different times according to their own clock, i.e. if one receiver measures at the clock's whole seconds while the other does not. The first point is easily adressed by double differencing the measurements, cancelling the receiver clock errors, but this does not handle the difference in measurement time. This is of less or no importance if higher grade receivers are used, that either steer their clock to the GNSS system time, or correct the clock often (i.e. every time a navigation solution is calculated) such that the clock error remains very small. For receivers used in today's consumer products, such as those made by U-Blox AG [11], the clocks are however free to drift within set thresholds on the millisecond level without being corrected. Only if the threshold is violated will a millisecond step correction be applied to the clock. This can lead to measurements being taken a few milliseconds apart. The handling of this is a necessary part of real-time kinematic positioning such as RTKLIB [12], where measurements from the base receiver can be delayed or sampled at a different rate than the rover measurements. [13] suggests time extrapolating the carrier phase measurements using the measured Doppler frequency shift, while [14] proposes a clock correction based on code-only least squares position and clock error estimates. [12] uses the estimated receiver velocity to correct the base station position before the baseline processing.

A. Main contribution

The main contribution of this paper is tightly coupled integration of dual receiver GPS L1 C/A measurements with inertial navigation using a multiplicative extended Kalman filter (MEKF) [15] (with the attitude error state based on the Gibbs vector), estimating the attitude as a unit quaternion in addition to position, velocity, IMU biases, carrier phase ambiguities and receiver clock offsets and drift rates. The difference in measurement time is explicitly included in the carrier phase measurement model as a function of the estimated vehicle state, also including this in the linearized model used for covariance correction. Thus the corrected smooth INS output is used for measurement time correction, unlike pure GNSS-based estimates or measurements in [13] and [14]. The lever arm of the receivers and the rotation-induced velocity is included in the measurement models, such that the estimated position and velocity is valid for the position of the IMU. The estimation algorithm is tested using data collected during a fixed-wing UAV flight.

The paper proceeds as follows: We first describe the measurement models used for the raw GNSS measurements and the interferometric use of carrier phase for measuring attitude. The compensation of differences in measurement time for carrier phase interferometry is described, before briefly introducing the multiplicative extended Kalman filter (MEKF) and the system dynamics model used. The measurement models used for the MEKF correction step is then presented. The carrier phase measurement model is formulated to take the difference in measurement times into account. Results from verification of the proposed method using the collected UAV flight data is then presented and discussed. Finally, the concluding marks are presented with suggestions for further work.

II. GNSS OBSERVABLES

1) Pseudorange: The pseudorange is the difference between the time of signal reception according to the receiver and the time of signal transmission according to the satellite, scaled to distance using the speed of light c. Receiver and satellite clock errors, ionospheric and tropospheric delays, multipath and other sources all cause errors in ranging. The true geometric range between the antenna of a satellite s and receiver α travelled by the signal in absence of atmospheric effects, using Earth Centered Earth Fixed (ECEF) coordinates, is

$$\rho_{\alpha,s}(t_{rx}) = \|\mathbf{R}^{e,rx}_{e,tx}\boldsymbol{p}^{e,tx}_{es}(t_{tx}) - \boldsymbol{p}^{e,rx}_{e\alpha}(t_{rx})\|_2, \quad (1)$$

$$= c(t_{rx} - t_{tx}), \quad (2)$$

where $\boldsymbol{p}^{e,rx}_{e\alpha}(t_{rx})$ is the position of the receiver antenna at the time of signal reception t_{rx}, given in the ECEF coordinate frame of the same time, $\{e, rx\}$, and $\boldsymbol{p}^{e,tx}_{es}(t_{tx})$ is the position of the satellite antenna at the time of signal transmission t_{tx} in the ECEF frame $\{e, tx\}$. The rotation matrix $\mathbf{R}^{e,rx}_{e,tx} = \mathbf{R}_z(\omega_{ie}(t_{rx} - t_{tx}))$ around the ECEF z-axis accounts for Earth rotation rate ω_{ie} during the signal propagation time, such that the positions used in the expression for range are in the same frame [16]. With the effects of ionospheric and tropospheric delays, and satellite and receiver clock errors included, the psedorange for a single satellite can be modelled as [17]

$$P_{\alpha,s}(t_{rx,\alpha}) = \rho_{\alpha,s}(t_{rx,\alpha}) + c(\delta t_\alpha(t_{rx,\alpha}) - \delta t_s(t_{tx,s})) + I_{\alpha,s} + T_{\alpha,s} + \epsilon_P, \quad (3)$$

where $P_{\alpha,s}$ is the measured pseudorange, δt_α and δt_s are the receiver and satellite clock errors, respectively, $I_{\alpha,s}$ and $T_{\alpha,s}$ are the ionospheric and tropospheric delays and ϵ_P is noise and unmodelled errors such as multipath. The times $t_{rx,\alpha} = t_{rx} + \delta t_\alpha$ and $t_{tx,s} = t_{tx} + \delta t_s$ are the time of the receiver and satellite clocks at the true times of reception and transmission. The time of transmission of the satellite clock can be found using the relation $t_{tx,s} = t_{rx,\alpha} - \frac{P}{c}$ and the true time can then be found by calculating the correction δt_s using parameters in the received navigation data.

2) Doppler frequency shift: The receiver tracks the carrier frequency of the received signal, often as a part of carrier phase tracking. The frequency received depends on the relative movement of the satellite and the receiver due to the Doppler shift. This raw measurement relates to the pseudorange P and carrier phase ϕ measurements as [16]

$$\dot{P} = \lambda\dot{\phi} = -\lambda\Delta f_{\mathrm{m}}, \tag{4}$$

where λ is the wavelength, and Δf_{m} is the difference between the measured carrier frequency and the nominal carrier frequency, $\Delta f_{\mathrm{m}} = f_{\text{measured}} - f_{L1}$. Because the rate of change of the ionospheric and tropospheric errors are small, we ommit these terms and use the model

$$\lambda\dot{\phi}_{\alpha,s}(t_{rx,\alpha}) = \dot{\rho}_{\alpha,s}(t_{rx,\alpha}) + c(\dot{\delta}t_{\alpha}(t_{rx,\alpha}) - \dot{\delta}t_{s}(t_{tx,s})) + \epsilon_{\dot{\phi}}. \tag{5}$$

Earth rotation also needs to be taken into consideration when using range rate to estimate the antenna velocity. The velocity contribution of the rotating ECEF frame relative to inertial space, with the lever arms from the center of the Earth, should be included in the model [16],

$$\dot{\rho}_{\alpha,s}(t_{rx}) = (\boldsymbol{l}^{e,rx})^{\top}\Big(\mathbf{R}^{e,rx}_{e,tx}(\boldsymbol{v}^{e,tx}_{es}(t_{tx}) + \mathbf{S}(\boldsymbol{\omega}^{e}_{ie})\boldsymbol{p}^{e,tx}_{es}(t_{tx})) - (\boldsymbol{v}^{e,rx}_{e\alpha}(t_{rx}) + \mathbf{S}(\boldsymbol{\omega}^{e}_{ie})\boldsymbol{p}^{e,rx}_{e\alpha}(t_{rx}))\Big), \tag{6}$$

where $\boldsymbol{l}^{e,rx}$ is the unit length line of sight (LOS) vector from $\boldsymbol{p}^{e,rx}_{e\alpha}(t_{rx})$ pointing towards $\boldsymbol{p}^{e,rx}_{es}(t_{tx})$.

3) Carrier phase: The carrier phase of the signal is tracked by phase lock loops (PLLs) in the receiver. The carrier phase measurement is based on the accumulation of Doppler frequency shift [18] in addition to fractional phase measurements [19], and the observable is therefore also known as accumulated Doppler range (ADR). Because the receiver only starts counting cycles from the time at which it locks onto the signal from each satellite, the carrier phase does not provide absolute range measurements, since the number of carrier cycles from satellite to receiver is unknown. The carrier phase measurement can be modelled as [16]

$$\lambda\phi_{\alpha,s} = \rho_{\alpha,s} + \lambda N_{\alpha,s} - I_{\alpha,s} + T_{\alpha,s} + c(\delta t_{\alpha} - \delta t_{s}) + b_{\alpha} - b_{s} + \phi_{p} + \phi_{M} + \epsilon_{\phi}, \tag{7}$$

written here without explicit times, where $N_{\alpha,s}$ is an integer number of carrier cycles, b_{α} and b_{s} are receiver and satellite LOS-independent phase biases with respect to the code, occuring in hardware, software and antennas, including phase-windup due to in-plane rotation of the antennas. ϕ_{p} is a LOS-dependent windup error, ϕ_{M} is an error due to signal multipath and signals received only via reflected paths, and ϵ_{ϕ} is the carrier phase tracking error. This model assumes that half cycle errors, caused by the data modulated onto the carrier, are resolved by the receiver after demodulating the data.

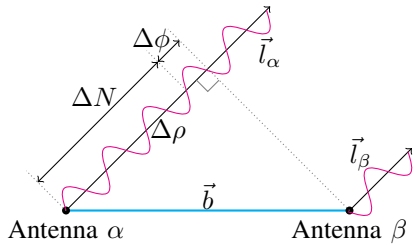

Fig. 1: Parallel LOS vectors. The LOS for receivers α and β, $\vec{l}_{\alpha}$ and $\vec{l}_{\beta}$, can be reasonably approximated as equal, $\vec{l}_{\alpha} \approx \vec{l}_{\beta}$. $\Delta\rho$ is the difference in range from each receiver to the satellite, which can be split into an integer wavelength part ΔN and a fractional part $\Delta\phi$.

III. Carrier phase interferometry

The use of multiple antennas for estimation of heading or attitude, for short baselines, can be done using an interferometric method with the measured carrier phase. Due to the large distance from a user to the medium Earth orbit (MEO) satellites, antennas fixed at different locations on a vehicle can be reasonably approximated as having parallel LOS vectors. This is illustrated in Fig. 1. This approximation means that the signal from a satellite can be seen as a plane wave. Because receivers can start tracking a satellite at different times, because cycle slips can occur causing the integer ambiguity to change, and because some receivers add an integer to the measurement in an attempt to align the measurement with the range measured using code, each of the components $\Delta\phi$ and ΔN in Fig. 1 will not necessarily be smaller in magnitude than the length of the baseline in cycles.

By differencing the carrier phase (7) between two receivers, called single differencing, we are able to cancel the satellite clock error and phase bias. Because the atmospheric errors are highly spatially correlated, the errors for two receivers mounted on the same vehicle is close to identical, such that these also can be considered to cancel each other. If the antennas are mounted with their planes in parallel, the LOS-dependent phase windup error also cancels for short baselines,

$$\begin{aligned}\lambda\Delta\phi_{\alpha\beta,s} &= \lambda(\phi_{\alpha,s} - \phi_{\beta,s}) \\ &= \Delta\rho_{\alpha\beta,s} + \lambda\Delta N_{\alpha\beta,s} + c(\delta t_{\alpha} - \delta t_{\beta}) \\ &\quad + b_{\alpha} - b_{\beta} + \Delta\phi_{M} + \Delta\epsilon_{\phi}.\end{aligned} \tag{8}$$

Furthermore, differencing (8) between two satellites s_1 and s_2, called double differencing, cancels errors common to the receivers, including the receiver clock errors and phase biases,

$$\begin{aligned}\lambda\nabla\Delta\phi_{\alpha\beta,s_1s_2} &= \lambda(\Delta\phi_{\alpha\beta,s_1} - \Delta\phi_{\alpha\beta,s_2}) \\ &= \nabla\Delta\rho_{\alpha\beta,s_1s_2} + \lambda\nabla\Delta N_{\alpha\beta,s_1s_2} \\ &\quad + \nabla\Delta\phi_{M} + \nabla\Delta\epsilon_{\phi}.\end{aligned} \tag{9}$$

The multipath and tracking errors do not cancel, and will be considered as disturbances. Because we normally track many satellites simultaneously, the differencing between satellites can be done in multiple ways. In general we can define a

differencing matrix $\mathbf{A} \in \mathbb{R}^{(k-1)\times k}$ for k single differenced measurements, with rows that sum to zero,

$$\lambda \mathbf{A} \Delta \boldsymbol{\phi}_{\alpha\beta} = \mathbf{A}(\Delta \boldsymbol{\rho}_{\alpha\beta} - \lambda \Delta \boldsymbol{N}_{\alpha\beta} + \Delta \boldsymbol{\epsilon}_{\phi}). \quad (10)$$

In the following, $\mathbf{A}$ will be chosen to use the highest elevation satellite as the reference to difference all other satellites against.

The range difference to a satellite between two receivers is the projection of the baseline vector $\vec{b}$ onto the LOS vector,

$$\Delta \rho_{\alpha\beta,s} = \vec{l}_s \cdot \vec{b} = \|\vec{b}\|_2 \cos \theta_{\vec{l}_s,\vec{b}}, \quad (11)$$

which in vector form can be written as

$$\Delta \boldsymbol{\rho}_{\alpha\beta} = \lambda(\Delta \boldsymbol{\phi}_{\alpha\beta} - \Delta \boldsymbol{N}_{\alpha\beta} - \Delta \boldsymbol{\epsilon}_{\phi}) = (\mathbf{L}^e)^\top \mathbf{R}_b^e \boldsymbol{b}^b, \quad (12)$$

with

$$\Delta \boldsymbol{\phi} = \left[\Delta\phi^1 \cdots \Delta\phi^k\right]^\top, \ \Delta \boldsymbol{N} = \left[\Delta N^1 \cdots \Delta N^k\right]^\top, \quad (13)$$

$$\mathbf{L}^e = \left[\boldsymbol{l}_1^e \ldots \boldsymbol{l}_k^e\right] \in \mathbb{R}^{3\times k}. \quad (14)$$

The equation being the basis for the MEKF measurement model for double differenced carrier phase (DDCP) is then

$$\mathbf{A}\lambda(\Delta \boldsymbol{\phi}_{\alpha\beta} - \Delta \boldsymbol{N}_{\alpha\beta} - \Delta \boldsymbol{\epsilon}_{\phi}) = \mathbf{A}(\mathbf{L}^e)^\top \mathbf{R}_b^e \boldsymbol{b}^b. \quad (15)$$

IV. Receiver Measurement Time Compensation

The carrier phase differencing in section III assumes that the measurements are taken at exactly the same time by both receivers. If measurement times are different, the satellites will move, satellite clocks will drift, and, for attitude determination cases like here, both receiver antennas can move in the interval between measurements. Note that the clock drift of the receivers in the period between measurements will cancel in double differencing and does not have to be considered. Using independent receivers, the best performance would be achieved if the measurement times could be steered to a common time (i.e. aligned with Global Positioning System Time (GPST)), but low-cost receivers typically do not do this [19]. Instead the error caused by different measurement times must be compensated afterwards using some form of correction term. The time of validity of the resulting state correction must be chosen, for example as the measurement time of one of the receivers or as a different time, i.e. aligned with GPST. Aligning with GPST has the advantage of making the validity time of the correction independent of the receiver clock errors, but requires two correction terms instead of one.

One possibility is to use the measured Doppler frequency shifts to extrapolate the carrier phase measurements to the chosen common time, using the approximation

$$\phi_\beta(t_\alpha) \approx \phi_\beta(t_\beta) + (t_\alpha - t_\beta)\dot{\phi}_\beta(t_\beta). \quad (16)$$

This has the advantage of simplicity, as the measurement model used in a Kalman filter does not have to consider the correction at all, but the Doppler measurement noise will then propagate to the extrapolated carrier phase. An example of this method on estimated double differenced ambiguity is shown in Fig. 2. Equivalently, an estimate of the carrier phase

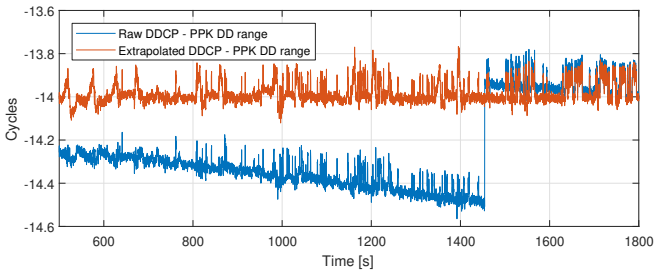

Fig. 2: Effect of differences in measurement time on DDCP: The differences between the measured DDCP, with and without correction for different measurement times (as shown in Fig. 5) for the two receivers, and the predicted double differenced (DD) range from post-processed kinematic (PPK) positioning are plotted. The blue uncorrected value is clearly affected by the clock drift of the two receivers. The red corrected value is very close to the integer value of -14 wavelength cycles.

rate based on the estimated vehicle state from the INS and the satellite states calculated using the ephemeris parameters, using (5), can be used for extrapolation, which can then also be included in the linearized measurement model used for gain calculation and covariance correction, as will be done in section VI-C. Simply including the extrapolation of the measurement(s) using modelled carrier phase rate will however also extrapolate the position and clock errors of the satellites, which is unneccessary as these values can be calculated at any time within the validity period of the ephemeris. Thus one could calculate the satellite positions and clock errors for the times needed, and only extrapolate the base antenna position. Consequently, for the case of real-time kinematic positioning where a fixed base antenna is used, no extrapolation is necessary as only the effect of satellite movement and clock drift must be considered, which is well predicted from the broadcast orbital and clock parameters and significant differences in measurement time can thus be handled. For the short time difference between receiver measurements however, the error caused by satellite position extrapolation is on the sub-micrometer level and thus considered negligible. Because the measurement output of a GNSS receiver are commonly more delayed than the output of an IMU, it is also possible to interpolate the INS-predicted position instead of extrapolating it, if the output rate of the IMU is high enough.

While low-cost receivers do not steer their internal clock to align with GPST, they can correct the clock in millisecond increments in order to keep it *approximately* aligned with GPST [20]. It must also be taken into consideration that the receivers do not necessarily schedule each measurement at the exact same time according to their own clock. The difference in the reported measurement time must be used in addition to the estimated clock errors. The combined difference for two receivers is

$$(t_\alpha - t_\beta) = \underbrace{t_{m\alpha} - t_{m\beta}}_{\text{Timestamps}} + \underbrace{\delta t_\beta - \delta t_\alpha}_{\text{Clock errors}}, \quad (17)$$

where $t_{m\alpha}$ and $t_{m\beta}$ are the receiver measurement timestamps.

V. MEKF

The multiplicative extendend Kalman filter [15] is an error state Kalman filter used for attitude estimation where the nominal part of the attitude is parametrized using the unit quaternion, while the error component is chosen as a three dimensional parametrization. After the initial transient the error component will be small, staying away from any singularities of the error parametrization, while having a covariance matrix with full rank. The estimator is therefore in practice globally nonsingular. The multiplicative part of the filter is the injection of the estimated error into the nominal estimate, which is done using the quaternion product [21]. Note that the error injection form can be chosen individually for the different states, such that the multiplicative error injection for attitude can be combined with the standard additive injection for other states.

A. IMU model

The measurement from the angular rate sensor is modelled as

$$\boldsymbol{\omega}^m_{\text{IMU}} = \mathbf{S}_g^{-1}\boldsymbol{\omega}^b_{ib} + \boldsymbol{b}^m_g + \boldsymbol{w}^m_g, \tag{18}$$

where $\boldsymbol{\omega}^b_{ib}$ is the angular rate of the body frame $\{b\}$ relative inertial space, approximated as the Earth Centered Inertial (ECI) frame $\{i\}$, $\mathbf{S}_g$ is the gyro calibration matrix which includes the orientation of the measurement frame $\{m\}$ relative $\{b\}$ as well as scale factor and non-orthogonality errors, $\boldsymbol{b}^m_g$ is a measurement bias, modelled as a Wiener process,

$$\dot{\boldsymbol{b}}^m_g = \boldsymbol{w}^m_{b_g}, \tag{19}$$

where $\boldsymbol{w}^m_g$ and $\boldsymbol{w}^m_{b_g}$ are Gaussian noise processes with the distributions

$$\boldsymbol{w}^m_g \sim \mathcal{N}(0, \sigma^2_g) \qquad \boldsymbol{w}^m_{b_g} \sim \mathcal{N}(0, \sigma^2_{b_g}), \tag{20}$$

which means that the noises are assumed isotropic, and the noise properties are independent of the decomposing axes. The accelerometer measurement is modelled as

$$\begin{aligned}\boldsymbol{f}^m_{\text{IMU}} &= \mathbf{S}_f^{-1}\boldsymbol{f}^b_{ib} + \boldsymbol{b}^m_a + \boldsymbol{w}^m_a &(21)\\ &= \mathbf{S}_f^{-1}(\boldsymbol{a}^b_{ib} - \boldsymbol{g}^b) + \boldsymbol{b}^m_a + \boldsymbol{w}^m_a &(22)\end{aligned}$$

where $\boldsymbol{f}^b_{ib}$ is the specific force on the sensor, given relative ECI, $\boldsymbol{a}^b_{ib}$ is the coordinate acceleration and $\boldsymbol{g}^m$ is the gravity vector. $\mathbf{S}_f$ is the accelerometer calibration matrix. Bias and noises are modelled as for the angular rate sensor,

$$\dot{\boldsymbol{b}}^m_a = \boldsymbol{w}^m_{b_a}, \tag{23}$$

$$\boldsymbol{w}^m_a \sim \mathcal{N}(0, \sigma^2_a) \qquad \boldsymbol{w}^m_{b_a} \sim \mathcal{N}(0, \sigma^2_{b_a}). \tag{24}$$

B. System kinematic model

As the ECEF frame is used by the Global Positioning System (GPS), it is a reasonable choice of reference frame also for the MEKF. The state vector representing the true values is chosen as

$$\boldsymbol{x} = [\boldsymbol{q}^{e\top}_b \ \boldsymbol{b}^{m\top}_g \ \boldsymbol{p}^{e\top}_{eb} \ \boldsymbol{v}^{e\top}_{eb} \ \boldsymbol{b}^{m\top}_a \ t_{\varepsilon f} \ t_{\varepsilon\beta} \ t_{df} \ t_{d\beta} \ \boldsymbol{N}^\top_{dd}]^\top, \tag{25}$$

where $\boldsymbol{q}^e_b \in \mathbb{R}^4$ is the unit quaternion describing the rotation between ECEF and the body frame, $\boldsymbol{b}^m_g$ and $\boldsymbol{b}^m_a$ are the biases in (18) and (22), $\boldsymbol{p}^e_{eb}$ and $\boldsymbol{v}^e_{eb}$ are the ECEF position and velocity vectors of the body frame origin (chosen as the location of the IMU), $t_{\varepsilon f}$ and $t_{\varepsilon\beta}$ are the clock offsets of the front and back receiver in unit of meters and t_{df} and $t_{d\beta}$ are the clock drift rates of the front and back receivers in unit of meters per second. $\boldsymbol{N}_{dd}$ are real-valued double differenced carrier phase ambiguities, which will vary in dimension as the number of tracked satellites change over time. The ambiguities are estimated as real-valued, before the LAMBDA algorithm [22] is used to find the best fitting integer vector. For the MEKF the state vector is split into a nominal component

$$\hat{\boldsymbol{x}} = [\hat{\boldsymbol{q}}^{e\top}_b \ \hat{\boldsymbol{b}}^{m\top}_g \ \hat{\boldsymbol{p}}^{e\top}_{eb} \ \hat{\boldsymbol{v}}^{e\top}_{eb} \ \hat{\boldsymbol{b}}^{m\top}_a \ \hat{t}_{\varepsilon f} \ \hat{t}_{\varepsilon\beta} \ \hat{t}_{df} \ \hat{t}_{d\beta} \ \hat{\boldsymbol{N}}^\top_{dd}]^\top, \tag{26}$$

where the $\hat{}$ operator indicates the expected value, and an error component

$$\delta\boldsymbol{x} = [\delta\boldsymbol{a}^\top \ \delta\boldsymbol{b}^{m\top}_g \ \delta\boldsymbol{p}^{e\top}_{eb} \ \delta\boldsymbol{v}^{e\top}_{eb} \ \delta\boldsymbol{b}^{m\top}_a \ \delta t_{\varepsilon f} \ \delta t_{\varepsilon\beta} \ \delta t_{df} \ \delta t_{d\beta} \ \delta\boldsymbol{N}^\top_{dd}]^\top, \tag{27}$$

where $\delta\boldsymbol{a}$ is the attitude error parametrized by twice the Gibbs vector [15],

$$\delta\boldsymbol{a} \coloneqq 2\frac{\delta\boldsymbol{\epsilon}}{\delta\eta}, \tag{28}$$

with $\delta\boldsymbol{\epsilon}$ being the imaginary vector part of the error quaternion $\delta\boldsymbol{q} = (\hat{\boldsymbol{q}}^e_b)^{-1} \otimes \boldsymbol{q}^e_b$, with $\otimes$ indicating the quaternion product [21], and $\delta\eta$ is the real scalar part. The nominal and error components relate to the true state using

$$\begin{aligned}
\boldsymbol{q}^e_b &= \hat{\boldsymbol{q}}^e_b \otimes \delta\boldsymbol{q}(\delta\boldsymbol{a}) & t_{\varepsilon f} &= \hat{t}_{\varepsilon f} + \delta t_{\varepsilon f}\\
\boldsymbol{b}^m_g &= \hat{\boldsymbol{b}}^m_g + \delta\boldsymbol{b}^m_g & t_{\varepsilon\beta} &= \hat{t}_{\varepsilon\beta} + \delta t_{\varepsilon\beta}\\
\boldsymbol{p}^e_{eb} &= \hat{\boldsymbol{p}}^e_{eb} + \delta\boldsymbol{p}^e_{eb} & t_{df} &= \hat{t}_{df} + \delta t_{df}\\
\boldsymbol{v}^e_{eb} &= \hat{\boldsymbol{v}}^e_{eb} + \delta\boldsymbol{v}^e_{eb} & t_{d\beta} &= \hat{t}_{d\beta} + \delta t_{d\beta}\\
\boldsymbol{b}^m_a &= \hat{\boldsymbol{b}}^m_a + \delta\boldsymbol{b}^m_a & \boldsymbol{N}_{dd} &= \hat{\boldsymbol{N}}_{dd} + \delta\boldsymbol{N}_{dd},
\end{aligned} \tag{29}$$

where the error quaternion can be calculated from $\delta\boldsymbol{a}$ using

$$\delta\boldsymbol{q}(\delta\boldsymbol{a}) = \frac{1}{\sqrt{4 + \|\delta\boldsymbol{a}\|^2_2}}\begin{bmatrix}2\\ \delta\boldsymbol{a}\end{bmatrix}. \tag{30}$$

1) True system dynamics: The attitude and translational kinematics using the true states are

$$\begin{aligned}\dot{\boldsymbol{q}}^e_b &= \frac{1}{2}\boldsymbol{q}^e_b \otimes \boldsymbol{\omega}^b_{eb}, &(31)\\ &= \frac{1}{2}\boldsymbol{q}^e_b \otimes (\mathbf{S}_g(\boldsymbol{\omega}^m_{\text{IMU}} - \boldsymbol{b}^m_g - \boldsymbol{w}^m_g) - \mathbf{R}(\boldsymbol{q}^e_b)^\top\boldsymbol{\omega}^e_{ie}), &(32)\end{aligned}$$

$$\begin{aligned}\dot{\boldsymbol{p}}^e_{eb} &= \boldsymbol{v}^e_{eb}, &(33)\\ \dot{\boldsymbol{v}}^e_{eb} &= \mathbf{R}(\boldsymbol{q}^e_b)\mathbf{S}_f(\boldsymbol{f}^m_{\text{IMU}} - \boldsymbol{b}^m_a - \boldsymbol{w}^m_a) + \boldsymbol{g}^e - 2\mathbf{S}(\boldsymbol{\omega}^e_{ie})\boldsymbol{v}^e_{eb}. &(34)\end{aligned}$$

Note that when the quaternion product notation $\otimes$ here involves a vector, the vector takes the place of the imaginary part of a quaternion, with the real part set to zero. The clock

offset and drift rates are assumed to behave as the models

$$\dot{t}_{\varepsilon f} = t_{df} + w_{t_{\varepsilon f}}, \quad w_{t_{\varepsilon,f}} \sim \mathcal{N}(0,\, \sigma^2_{t_{\varepsilon f}}) \tag{35}$$

$$\dot{t}_{\varepsilon \beta} = t_{d\beta} + w_{t_{\varepsilon \beta}}, \quad w_{t_{\varepsilon,\beta}} \sim \mathcal{N}(0,\, \sigma^2_{t_{\varepsilon \beta}}) \tag{36}$$

$$\dot{t}_{df} = w_{t_{df}}, \qquad w_{t_{d,f}} \sim \mathcal{N}(0,\, \sigma^2_{t_{df}}) \tag{37}$$

$$\dot{t}_{d\beta} = w_{t_{d\beta}}, \qquad w_{t_{d,b}} \sim \mathcal{N}(0,\, \sigma^2_{t_{d\beta}}) \tag{38}$$

and the IMU biases, chosen to be decomposed in the measurement frame, have the models (19), (23). The ambiguity state is modelled as a slowly varying Wiener process,

$$\dot{\boldsymbol{N}}_{dd} = \boldsymbol{w}_{\boldsymbol{N}}, \quad \boldsymbol{w}_{\boldsymbol{N}} \sim \mathcal{N}(0,\, \sigma^2_{\boldsymbol{N}}). \tag{39}$$

2) Nominal dynamics: The dynamics of the nominal component of the state vector is simply the expected value of the true dynamics, which means that the states are replaced with their expected value and all noises are set to zero. The IMU used was configured to output velocity and angle increments, $\Delta \boldsymbol{v}^m_{\text{IMU}}$ and $\Delta \boldsymbol{\theta}^m_{\text{IMU}}$ at a rate of 250 Hz. The use of increments means that the internal high rate samples are integrated to provide lower rate outputs maintaining all information. The mechanization equations are implemented in discrete form as

$$\hat{\boldsymbol{a}}^e_{eb}\Delta t = \mathbf{R}(\hat{\boldsymbol{q}}^e_b)\mathbf{S}_f(\Delta \boldsymbol{v}^m_{\text{IMU}} - \hat{\boldsymbol{b}}^m_a \Delta t) + \boldsymbol{g}^e \Delta t - 2\mathbf{S}(\boldsymbol{\omega}^e_{ie})\hat{\boldsymbol{v}}^e_{eb}\Delta t \tag{40}$$

$$\hat{\boldsymbol{p}}^e_{eb} \leftarrow \hat{\boldsymbol{p}}^e_{eb} + \hat{\boldsymbol{v}}^e_{eb}\Delta t + \hat{\boldsymbol{a}}^e_{eb}\frac{\Delta t^2}{2} \tag{41}$$

$$\hat{\boldsymbol{v}}^e_{eb} \leftarrow \hat{\boldsymbol{v}}^e_{eb} + \hat{\boldsymbol{a}}^e_{eb}\Delta t \tag{42}$$

$$\Delta\hat{\boldsymbol{\theta}}^b \coloneqq \mathbf{S}_g(\Delta \boldsymbol{\theta}^m_{\text{IMU}} - \hat{\boldsymbol{b}}^m_g \Delta t) - \mathbf{R}(\hat{\boldsymbol{q}}^e_b)^\top \boldsymbol{\omega}^e_{ie} \tag{43}$$

$$\boldsymbol{q}(\Delta\hat{\boldsymbol{\theta}}^b) = \begin{bmatrix} \cos\left(\frac{\|\Delta\hat{\boldsymbol{\theta}}^b\|}{2}\right) \\ \frac{\Delta\hat{\boldsymbol{\theta}}^b}{\|\Delta\hat{\boldsymbol{\theta}}^b\|}\sin\left(\frac{\|\Delta\hat{\boldsymbol{\theta}}^b\|}{2}\right) \end{bmatrix} \tag{44}$$

$$\hat{\boldsymbol{q}}^e_b \leftarrow \hat{\boldsymbol{q}}^e_b \otimes \boldsymbol{q}(\Delta\hat{\boldsymbol{\theta}}) \tag{45}$$

$$\hat{t}_{\varepsilon f} \leftarrow \hat{t}_{\varepsilon f} + \hat{t}_{df}\Delta t \tag{46}$$

$$\hat{t}_{\varepsilon \beta} \leftarrow \hat{t}_{\varepsilon \beta} + \hat{t}_{d\beta}\Delta t \tag{47}$$

3) Error state dynamics: Since the expected error before a measurement is always zero, and the observed error is injected into the nominal state after a measurement, the expected error is zero at every timstep and the state prediction step of the Kalman filter does therefore not have to be implemented. The linearized error dynamics are however still needed for covariance propagation. From [15] we have the attitude error dynamics

$$\delta\dot{\boldsymbol{a}} = \Delta\boldsymbol{\omega} - \hat{\boldsymbol{\omega}}^b_{eb} \times \delta\boldsymbol{a} - \frac{1}{2}\Delta\boldsymbol{\omega} \times \delta\boldsymbol{a} + \frac{1}{4}(\Delta\boldsymbol{\omega} \cdot \delta\boldsymbol{a})\delta\boldsymbol{a} \tag{48}$$

with $\Delta\boldsymbol{\omega}$ extended with the effect of the Earth rotation,

$$\Delta\boldsymbol{\omega} = -\mathbf{S}_g\delta\boldsymbol{b}^m_g - \mathbf{S}_g\boldsymbol{w}_g + \mathbf{R}(\hat{\boldsymbol{q}}^e_b)^\top\boldsymbol{\omega}^e_{ie} - \mathbf{R}(\boldsymbol{q}^e_b)^\top\boldsymbol{\omega}^e_{ie}. \tag{49}$$

The translational error dynamics are

$$\delta\dot{\boldsymbol{p}}^e_{eb} = \delta\boldsymbol{v}^e_{eb}. \tag{50}$$

$$\delta\dot{\boldsymbol{v}}^e_{eb} = -2\mathbf{S}(\boldsymbol{\omega}^e_{ie})\delta\boldsymbol{v}^e_{eb} + (\mathbf{R}(\boldsymbol{q}^e_b) - \mathbf{R}(\hat{\boldsymbol{q}}^e_b))\mathbf{S}_f(\boldsymbol{f}^m_{\text{IMU}} - \hat{\boldsymbol{b}}^m_a) - \mathbf{R}(\boldsymbol{q}^e_b)\mathbf{S}_f(\delta\boldsymbol{b}^m_a + \boldsymbol{w}^m_a). \tag{51}$$

The error dynamics for the remaining biases, clock errors and ambiguity states are simply given by their process noises. These equations are linearized in order to find the linear system matrix $\mathbf{F}$. For attitude it is used that $\mathbf{R}(\boldsymbol{q}^e_b) = \mathbf{R}(\hat{\boldsymbol{q}}^e_b)\mathbf{R}(\delta\boldsymbol{a})$ and the first order approximation $\mathbf{R}(\delta\boldsymbol{a}) \approx \mathbf{I}_{3\times3} + \mathbf{S}(\delta\boldsymbol{a})$. The resulting linearized, continous time system matrix $\bar{\mathbf{F}}$ associated with the fixed part of the state vector, without the variable size ambiguity vector, is given in (52),

$$\bar{\mathbf{F}} = \begin{bmatrix}
-\mathbf{S}(\hat{\boldsymbol{\omega}}^b_{ib}) & -\mathbf{S}_g & \mathbf{0}_{3\times3} & \mathbf{0}_{3\times3} & \mathbf{0}_{3\times3} & \mathbf{0}_{3\times1} & \mathbf{0}_{3\times1} & \mathbf{0}_{3\times1} & \mathbf{0}_{3\times1} \\
\mathbf{0}_{3\times3} & \mathbf{0}_{3\times3} & \mathbf{0}_{3\times3} & \mathbf{0}_{3\times3} & \mathbf{0}_{3\times3} & \mathbf{0}_{3\times1} & \mathbf{0}_{3\times1} & \mathbf{0}_{3\times1} & \mathbf{0}_{3\times1} \\
\mathbf{0}_{3\times3} & \mathbf{0}_{3\times3} & \mathbf{0}_{3\times3} & \mathbf{I}_{3\times3} & \mathbf{0}_{3\times3} & \mathbf{0}_{3\times1} & \mathbf{0}_{3\times1} & \mathbf{0}_{3\times1} & \mathbf{0}_{3\times1} \\
-\mathbf{R}(\hat{\boldsymbol{q}}^e_b)\mathbf{S}(\hat{\boldsymbol{f}}^b_{ib}) & \mathbf{0}_{3\times3} & \mathbf{0}_{3\times3} & -2\mathbf{S}(\boldsymbol{\omega}^e_{ie}) & -\mathbf{R}(\hat{\boldsymbol{q}}^e_b)\mathbf{S}_f & \mathbf{0}_{3\times1} & \mathbf{0}_{3\times1} & \mathbf{0}_{3\times1} & \mathbf{0}_{3\times1} \\
\mathbf{0}_{3\times3} & \mathbf{0}_{3\times3} & \mathbf{0}_{3\times3} & \mathbf{0}_{3\times3} & \mathbf{0}_{3\times3} & \mathbf{0}_{3\times1} & \mathbf{0}_{3\times1} & \mathbf{0}_{3\times1} & \mathbf{0}_{3\times1} \\
\mathbf{0}_{1\times3} & \mathbf{0}_{1\times3} & \mathbf{0}_{1\times3} & \mathbf{0}_{1\times3} & \mathbf{0}_{1\times3} & 0 & 0 & 1 & 0 \\
\mathbf{0}_{1\times3} & \mathbf{0}_{1\times3} & \mathbf{0}_{1\times3} & \mathbf{0}_{1\times3} & \mathbf{0}_{1\times3} & 0 & 0 & 0 & 1 \\
\mathbf{0}_{1\times3} & \mathbf{0}_{1\times3} & \mathbf{0}_{1\times3} & \mathbf{0}_{1\times3} & \mathbf{0}_{1\times3} & 0 & 0 & 0 & 0 \\
\mathbf{0}_{1\times3} & \mathbf{0}_{1\times3} & \mathbf{0}_{1\times3} & \mathbf{0}_{1\times3} & \mathbf{0}_{1\times3} & 0 & 0 & 0 & 0
\end{bmatrix}. \tag{52}$$

Combining this with the zero dynamics of the double differenced ambiguity errors, we get the complete matrix

$$\mathbf{F} = \begin{bmatrix} \bar{\mathbf{F}} & \mathbf{0}_{19\times(k-1)} \\ \mathbf{0}_{(k-1)\times19} & \mathbf{0}_{(k-1)\times(k-1)} \end{bmatrix} \in \mathbb{R}^{(19+k-1)\times(19+k-1)}. \tag{53}$$

The process noise input matrix for the fixed part of the error state is

$$\bar{\mathbf{G}} = \begin{bmatrix}
-\mathbf{S}_g & \mathbf{0}_{3\times3} & \mathbf{0}_{3\times3} & \mathbf{0}_{3\times3} & \mathbf{0}_{3\times1} & \mathbf{0}_{3\times1} & \mathbf{0}_{3\times1} & \mathbf{0}_{3\times1} \\
\mathbf{0}_{3\times3} & \mathbf{I}_{3\times3} & \mathbf{0}_{3\times3} & \mathbf{0}_{3\times3} & \mathbf{0}_{3\times1} & \mathbf{0}_{3\times1} & \mathbf{0}_{3\times1} & \mathbf{0}_{3\times1} \\
\mathbf{0}_{3\times3} & \mathbf{0}_{3\times3} & \mathbf{0}_{3\times3} & \mathbf{0}_{3\times3} & \mathbf{0}_{3\times1} & \mathbf{0}_{3\times1} & \mathbf{0}_{3\times1} & \mathbf{0}_{3\times1} \\
\mathbf{0}_{3\times3} & \mathbf{0}_{3\times3} & -\mathbf{S}_f & \mathbf{0}_{3\times3} & \mathbf{0}_{3\times1} & \mathbf{0}_{3\times1} & \mathbf{0}_{3\times1} & \mathbf{0}_{3\times1} \\
\mathbf{0}_{3\times3} & \mathbf{0}_{3\times3} & \mathbf{0}_{3\times3} & \mathbf{I}_{3\times3} & \mathbf{0}_{3\times1} & \mathbf{0}_{3\times1} & \mathbf{0}_{3\times1} & \mathbf{0}_{3\times1} \\
\mathbf{0}_{1\times3} & \mathbf{0}_{1\times3} & \mathbf{0}_{1\times3} & \mathbf{0}_{1\times3} & 1 & 0 & 0 & 0 \\
\mathbf{0}_{1\times3} & \mathbf{0}_{1\times3} & \mathbf{0}_{1\times3} & \mathbf{0}_{1\times3} & 0 & 1 & 0 & 0 \\
\mathbf{0}_{1\times3} & \mathbf{0}_{1\times3} & \mathbf{0}_{1\times3} & \mathbf{0}_{1\times3} & 0 & 0 & 1 & 0 \\
\mathbf{0}_{1\times3} & \mathbf{0}_{1\times3} & \mathbf{0}_{1\times3} & \mathbf{0}_{1\times3} & 0 & 0 & 0 & 1
\end{bmatrix}, \tag{54}$$

and the complete matrix including the ambiguities is

$$\mathbf{G} = \begin{bmatrix} \bar{\mathbf{G}} & \mathbf{0}_{19\times(k-1)} \\ \mathbf{0}_{(k-1)\times16} & \mathbf{I}_{(k-1)\times(k-1)} \end{bmatrix} \in \mathbb{R}^{(19+k-1)\times(16+k-1)}. \tag{55}$$

The linear process model is then

$$\delta\dot{\boldsymbol{x}} = \mathbf{F}\delta\boldsymbol{x} + \mathbf{G}\boldsymbol{w}, \tag{56}$$

where the noise vector is

$$\boldsymbol{w} = [\boldsymbol{w}_g^\top \;\; \boldsymbol{w}_{bg}^\top \;\; \boldsymbol{w}_a^\top \;\; \boldsymbol{w}_{ba}^\top \;\; w_{t_{\varepsilon f}} \;\; w_{t_{\varepsilon \beta}} \;\; w_{t_{df}} \;\; w_{t_{d\beta}} \;\; \boldsymbol{w}_N^\top]^\top. \tag{57}$$

The discrete time equivalents of $\mathbf{F}$ and $\mathbf{G}$ are found using Van Loan's method [23].

VI. Measurement models

For the measurements from each receiver, we take into account that the antenna positions are offset from the body frame coordinate origin, defined at the position of the IMU, by the vectors $\boldsymbol{r}^b_f$ and $\boldsymbol{r}^b_\beta$,

$$\boldsymbol{p}^e_{eb,f} = \boldsymbol{p}^e_{eb} + \mathbf{R}(\boldsymbol{q}^e_b)\boldsymbol{r}^b_f, \tag{58}$$

$$\boldsymbol{p}^e_{eb,\beta} = \boldsymbol{p}^e_{eb} + \mathbf{R}(\boldsymbol{q}^e_b)\boldsymbol{r}^b_\beta. \tag{59}$$

The velocity of each receiver is then

$$\boldsymbol{v}^e_{eb,f} = \boldsymbol{v}^e_{eb} + \mathbf{R}(\boldsymbol{q}^e_b)\mathbf{S}(\boldsymbol{\omega}^b_{eb})\boldsymbol{r}^b_f, \tag{60}$$

$$\boldsymbol{v}^e_{eb,\beta} = \boldsymbol{v}^e_{eb} + \mathbf{R}(\boldsymbol{q}^e_b)\mathbf{S}(\boldsymbol{\omega}^b_{eb})\boldsymbol{r}^b_\beta. \tag{61}$$

In the following the frame $\{e\}$ denotes the ECEF frame of the time of reception, $\{e, rx\}$.

A. Pseudorange

As a function of the vehicle state, using the lever arm, the pseudorange model (3) of the front receiver is written as

$$P_f = \|\hat{\mathbf{R}}^e_{e,tx}\boldsymbol{p}^{e,tx}_{es} - (\boldsymbol{p}^e_{eb} + \mathbf{R}(\boldsymbol{q}^e_b)\boldsymbol{r}^b_f)\|_2 + t_{\varepsilon f} + \epsilon_P + I + T - c\delta t_s. \tag{62}$$

where δt_s is the clock error computed from the correction parameters in the satellite navigation message [24] along with the satellite position $p^{e,tx}_{es}$ at the corrected time of signal transmission. I and T are values for the ionospheric delay from the Klobuchar [25] ionospheric model and the NATO STANAG tropospheric model [16]. Linearizing the model at the expected zero error, for a vector of k measurements, for each receiver, the linear measurement matrices become

$$\mathbf{H}_{P,f} = \begin{bmatrix} \hat{\boldsymbol{l}}^\top_{f,1}\mathbf{R}(\hat{\boldsymbol{q}}^e_b)\mathbf{S}(r^b_f) & \mathbf{0}_{1\times3} & -\hat{\boldsymbol{l}}^\top_{f,1} & \mathbf{0}_{1\times3} & \mathbf{0}_{1\times3} & 1 & 0 & 0 & 0 & \mathbf{0}_{1\times(k-1)} \\ \hat{\boldsymbol{l}}^\top_{f,2}\mathbf{R}(\hat{\boldsymbol{q}}^e_b)\mathbf{S}(r^b_f) & \mathbf{0}_{1\times3} & -\hat{\boldsymbol{l}}^\top_{f,2} & \mathbf{0}_{1\times3} & \mathbf{0}_{1\times3} & 1 & 0 & 0 & 0 & \mathbf{0}_{1\times(k-1)} \\ & & & & \vdots & & & & & \\ \hat{\boldsymbol{l}}^\top_{f,k}\mathbf{R}(\hat{\boldsymbol{q}}^e_b)\mathbf{S}(r^b_f) & \mathbf{0}_{1\times3} & -\hat{\boldsymbol{l}}^\top_{f,k} & \mathbf{0}_{1\times3} & \mathbf{0}_{1\times3} & 1 & 0 & 0 & 0 & \mathbf{0}_{1\times(k-1)} \end{bmatrix}, \tag{63}$$

$$\mathbf{H}_{P,\beta} = \begin{bmatrix} \hat{\boldsymbol{l}}^\top_{\beta,1}\mathbf{R}(\hat{\boldsymbol{q}}^e_b)\mathbf{S}(r^b_\beta) & \mathbf{0}_{1\times3} & -\hat{\boldsymbol{l}}^\top_{\beta,1} & \mathbf{0}_{1\times3} & \mathbf{0}_{1\times3} & 0 & 1 & 0 & 0 & \mathbf{0}_{1\times(k-1)} \\ \hat{\boldsymbol{l}}^\top_{\beta,2}\mathbf{R}(\hat{\boldsymbol{q}}^e_b)\mathbf{S}(r^b_\beta) & \mathbf{0}_{1\times3} & -\hat{\boldsymbol{l}}^\top_{\beta,2} & \mathbf{0}_{1\times3} & \mathbf{0}_{1\times3} & 0 & 1 & 0 & 0 & \mathbf{0}_{1\times(k-1)} \\ & & & & \vdots & & & & & \\ \hat{\boldsymbol{l}}^\top_{\beta,k}\mathbf{R}(\hat{\boldsymbol{q}}^e_b)\mathbf{S}(r^b_\beta) & \mathbf{0}_{1\times3} & -\hat{\boldsymbol{l}}^\top_{\beta,k} & \mathbf{0}_{1\times3} & \mathbf{0}_{1\times3} & 0 & 1 & 0 & 0 & \mathbf{0}_{1\times(k-1)} \end{bmatrix}, \tag{64}$$

each $\in \mathbb{R}^{k\times(19+k-1)}$.

B. Doppler

Using (4) and (5) and the antenna velocity (60), the Doppler measurement can be written as

$$\lambda\Delta f_f = \boldsymbol{l}^{e\top}_f\Big(\boldsymbol{v}^e_{eb} + \mathbf{R}(\boldsymbol{q}^e_b)\mathbf{S}(\boldsymbol{\omega}^b_{eb})\boldsymbol{r}^b_f + \mathbf{S}(\boldsymbol{\omega}^e_{ie})\boldsymbol{p}^e_{eb} - \hat{\mathbf{R}}^e_{e,tx}\big(\boldsymbol{v}^{e,tx}_{es} - \mathbf{S}(\boldsymbol{\omega}^e_{ie})\boldsymbol{p}^{e,tx}_{es}\big)\Big) - t_{df} + c\delta\dot{t}_s + \epsilon_{\Delta f}. \tag{65}$$

The dependency of the model on position errors through the Earth rotation rate and the dependency on position and attitude errors throught the LOS-vector are ignored as these terms are negligible due to the slow Earth-rotation rate and low sensitivity of the LOS vector to small position errors. The linearization of the model at the expected zero error gives the measurement matrices (72), (73).

C. Double differenced carrier phase

The carrier phase measurement matrix will be constructed first for the fixed part of the state vector, $\bar{\boldsymbol{x}}$, for single differenced measurements, with the corresponding double differenced measurement matrix then simply calculated as

$$\mathbf{H}_{dd,\bar{\boldsymbol{x}}} = \mathbf{A}\mathbf{H}_{sd,\bar{\boldsymbol{x}}}. \tag{66}$$

The complete double differenced measurement matrix including the double differenced ambiguities is then

$$\mathbf{H}_{dd} = \begin{bmatrix}\mathbf{H}_{dd,\bar{\boldsymbol{x}}} & \mathbf{I}_{(k-1)\times(k-1)}\end{bmatrix} \in \mathbb{R}^{(k-1)\times(19+k-1)}. \tag{67}$$

Using the linear time extrapolation with the measurement time of the front receiver chosen as the time of differencing, the single differenced measurement model becomes

$$\phi_\beta + (t_f - t_\beta)\dot{\phi}_\beta - \phi_f = \frac{1}{\lambda}\boldsymbol{l}^{e\top}\mathbf{R}(\boldsymbol{q}^e_b)\boldsymbol{b}^b + N_{sd}. \tag{68}$$

Substituting in the expression for the carrier phase derivative using (65) and (4) gives

$$\begin{aligned}\phi_\beta - \phi_f &= \frac{1}{\lambda}\boldsymbol{l}^{e\top}\mathbf{R}(\boldsymbol{q}^e_b)\boldsymbol{b}^b + N_{sd} \\ &+ (t_f - t_\beta)\frac{1}{\lambda}\Big(\boldsymbol{l}^{e\top}(\boldsymbol{v}^e_{eb} + \mathbf{R}(\boldsymbol{q}^e_b)\mathbf{S}(\boldsymbol{\omega}^b_{eb})\boldsymbol{r}^b_\beta + \mathbf{S}(\boldsymbol{\omega}^e_{ie})\boldsymbol{p}^e_{eb} \\ &- \hat{\mathbf{R}}^e_{e,tx}\big(\boldsymbol{v}^{e,tx}_{es} - \mathbf{S}(\boldsymbol{\omega}^e_{ie})\boldsymbol{p}^{e,tx}_{es}\big)\Big) - t_{d\beta} + c\dot{\delta t}_s + \epsilon_{\Delta f}\Big) + \epsilon_{\phi_{sd}}.\end{aligned} \tag{69}$$

Note that because we will difference the model between satellites later, terms that are the same for all satellites will cancel, in this case this only applies to the drift rate $t_{d\beta}$, which will therefore be ignored in the following derivatives. The derivative with respect to the attitude error is

$$\frac{\partial\Delta\phi_{\beta f}}{\partial\delta\boldsymbol{a}} = -\frac{1}{\lambda}\boldsymbol{l}^{e\top}\mathbf{R}(\hat{\boldsymbol{q}}^e_b)\Big(\mathbf{S}(\boldsymbol{b}^b) - (t_f - t_\beta)\mathbf{S}(\mathbf{S}(\boldsymbol{\omega}^b_{eb})\boldsymbol{r}_\beta)\Big). \tag{70}$$

The angular rate $\boldsymbol{\omega}^b_{eb}$ makes the model dependent on the gyro bias. Differentiating with respect the gyro bias error gives

$$\frac{\partial\Delta\phi_{\beta f}}{\partial\delta\boldsymbol{b}^m_g} = \frac{t_f - t_\beta}{\lambda}\boldsymbol{l}^{e\top}\mathbf{R}(\boldsymbol{q}^e_b)\mathbf{S}(r_\beta)\mathbf{S}_g. \tag{71}$$

$$\mathbf{H}_{\Delta f,f} = \begin{bmatrix} -\hat{\boldsymbol{l}}^{e\top}_{f,1}\mathbf{R}(\hat{\boldsymbol{q}}^e_b)\mathbf{S}(\mathbf{S}(\hat{\boldsymbol{\omega}}^b_{eb})r^b_f) & \hat{\boldsymbol{l}}^{e\top}_{f,1}\mathbf{R}(\hat{\boldsymbol{q}}^e_b)\mathbf{S}(r^b_f)\mathbf{S}_g & \mathbf{0}_{1\times3} & \hat{\boldsymbol{l}}^{e\top}_{f,1} & \mathbf{0}_{1\times3} & 0 & 0 & -1 & 0 & \mathbf{0}_{1\times(k-1)} \\ -\hat{\boldsymbol{l}}^{e\top}_{f,2}\mathbf{R}(\hat{\boldsymbol{q}}^e_b)\mathbf{S}(\mathbf{S}(\hat{\boldsymbol{\omega}}^b_{eb})r^b_f) & \hat{\boldsymbol{l}}^{e\top}_{f,2}\mathbf{R}(\hat{\boldsymbol{q}}^e_b)\mathbf{S}(r^b_f)\mathbf{S}_g & \mathbf{0}_{1\times3} & \hat{\boldsymbol{l}}^{e\top}_{f,2} & \mathbf{0}_{1\times3} & 0 & 0 & -1 & 0 & \mathbf{0}_{1\times(k-1)} \\ & & & & & \vdots & & & & \\ -\hat{\boldsymbol{l}}^{e\top}_{f,k}\mathbf{R}(\hat{\boldsymbol{q}}^e_b)\mathbf{S}(\mathbf{S}(\hat{\boldsymbol{\omega}}^b_{eb})r^b_f) & \hat{\boldsymbol{l}}^{e\top}_{f,k}\mathbf{R}(\hat{\boldsymbol{q}}^e_b)\mathbf{S}(r^b_f)\mathbf{S}_g & \mathbf{0}_{1\times3} & \hat{\boldsymbol{l}}^{e\top}_{f,k} & \mathbf{0}_{1\times3} & 0 & 0 & -1 & 0 & \mathbf{0}_{1\times(k-1)} \end{bmatrix} \in \mathbb{R}^{k\times(19+k-1)}, \tag{72}$$

$$\mathbf{H}_{\Delta f,\beta} = \begin{bmatrix} -\hat{\boldsymbol{l}}^{e\top}_{\beta,1}\mathbf{R}(\hat{\boldsymbol{q}}^e_b)\mathbf{S}(\mathbf{S}(\hat{\boldsymbol{\omega}}^b_{eb})r^b_\beta) & \hat{\boldsymbol{l}}^{e\top}_{\beta,1}\mathbf{R}(\hat{\boldsymbol{q}}^e_b)\mathbf{S}(r^b_\beta)\mathbf{S}_g & \mathbf{0}_{1\times3} & \hat{\boldsymbol{l}}^{e\top}_{\beta,1} & \mathbf{0}_{1\times3} & 0 & 0 & 0 & -1 & \mathbf{0}_{1\times(k-1)} \\ -\hat{\boldsymbol{l}}^{e\top}_{\beta,2}\mathbf{R}(\hat{\boldsymbol{q}}^e_b)\mathbf{S}(\mathbf{S}(\hat{\boldsymbol{\omega}}^b_{eb})r^b_\beta) & \hat{\boldsymbol{l}}^{e\top}_{\beta,2}\mathbf{R}(\hat{\boldsymbol{q}}^e_b)\mathbf{S}(r^b_\beta)\mathbf{S}_g & \mathbf{0}_{1\times3} & \hat{\boldsymbol{l}}^{e\top}_{\beta,2} & \mathbf{0}_{1\times3} & 0 & 0 & 0 & -1 & \mathbf{0}_{1\times(k-1)} \\ & & & & & \vdots & & & & \\ -\hat{\boldsymbol{l}}^{e\top}_{\beta,k}\mathbf{R}(\hat{\boldsymbol{q}}^e_b)\mathbf{S}(\mathbf{S}(\hat{\boldsymbol{\omega}}^b_{eb})r^b_\beta) & \hat{\boldsymbol{l}}^{e\top}_{\beta,k}\mathbf{R}(\hat{\boldsymbol{q}}^e_b)\mathbf{S}(r^b_\beta)\mathbf{S}_g & \mathbf{0}_{1\times3} & \hat{\boldsymbol{l}}^{e\top}_{\beta,k} & \mathbf{0}_{1\times3} & 0 & 0 & 0 & -1 & \mathbf{0}_{1\times(k-1)} \end{bmatrix} \in \mathbb{R}^{k\times(19+k-1)}. \tag{73}$$

Differentiating with respect to the clock biases, using (17), gives

$$\frac{\partial \Delta\phi_{\beta f}}{\partial \delta \boldsymbol{t}_{\varepsilon f}} = -\frac{1}{c\lambda}\Big(\boldsymbol{l}^{e\top}(\boldsymbol{v}^e_{eb} + \mathbf{R}(\boldsymbol{q}^e_b)\mathbf{S}(\boldsymbol{\omega}^b_{eb})\boldsymbol{r}^b_\beta + \mathbf{S}(\boldsymbol{\omega}^e_{ie})\boldsymbol{p}^e_{eb} - \hat{\mathbf{R}}^e_{e,tx}\big(\boldsymbol{v}^{e,tx}_{es} - \mathbf{S}(\boldsymbol{\omega}^e_{ie})\boldsymbol{p}^{e,tx}_{es}\big)) + c\delta\dot{t}_s + \epsilon_{\Delta f}\Big), \tag{74}$$

$$\frac{\partial \Delta\phi_{\beta f}}{\partial \delta \boldsymbol{t}_{\varepsilon \beta}} = -\frac{\partial \Delta\phi_{\beta f}}{\partial \delta \boldsymbol{t}_{\varepsilon f}}. \tag{75}$$

With respect to the velocity we have

$$\frac{\partial \Delta\phi_{\beta f}}{\partial \delta \boldsymbol{v}^e_{eb}} = (t_f - t_\beta)\frac{1}{\lambda}\boldsymbol{l}^{e\top}. \tag{76}$$

Writing $\Delta\phi_{\beta f}$ for satellite i as $\Delta\phi_i$ and using expected values, these can be combined to the matrix

$$\mathbf{H}_{sd,\bar{\boldsymbol{x}}} = \begin{bmatrix} \widehat{\frac{\partial\Delta\phi_1}{\partial \boldsymbol{a}}} & \widehat{\frac{\partial\Delta\phi_1}{\partial \delta \boldsymbol{b}_g}} & \mathbf{0}_{1\times3} & \widehat{\frac{\partial\Delta\phi_1}{\partial \delta \boldsymbol{v}^e_{eb}}} & \mathbf{0}_{1\times3} & \widehat{\frac{\partial\Delta\phi_1}{\partial \delta \boldsymbol{t}_{\varepsilon f}}} & \widehat{\frac{\partial\Delta\phi_1}{\partial \delta \boldsymbol{t}_{\varepsilon \beta}}} & 0 & 0 \\ \widehat{\frac{\partial\Delta\phi_2}{\partial \boldsymbol{a}}} & \widehat{\frac{\partial\Delta\phi_2}{\partial \delta \boldsymbol{b}_g}} & \mathbf{0}_{1\times3} & \widehat{\frac{\partial\Delta\phi_2}{\partial \delta \boldsymbol{v}^e_{eb}}} & \mathbf{0}_{1\times3} & \widehat{\frac{\partial\Delta\phi_2}{\partial \delta \boldsymbol{t}_{\varepsilon f}}} & \widehat{\frac{\partial\Delta\phi_2}{\partial \delta \boldsymbol{t}_{\varepsilon \beta}}} & 0 & 0 \\ & & & \vdots & & & & & \\ \widehat{\frac{\partial\Delta\phi_k}{\partial \boldsymbol{a}}} & \widehat{\frac{\partial\Delta\phi_k}{\partial \delta \boldsymbol{b}_g}} & \mathbf{0}_{1\times3} & \widehat{\frac{\partial\Delta\phi_k}{\partial \delta \boldsymbol{v}^e_{eb}}} & \mathbf{0}_{1\times3} & \widehat{\frac{\partial\Delta\phi_k}{\partial \delta \boldsymbol{t}_{\varepsilon f}}} & \widehat{\frac{\partial\Delta\phi_k}{\partial \delta \boldsymbol{t}_{\varepsilon \beta}}} & 0 & 0 \end{bmatrix} \tag{77}$$

$\in \mathbb{R}^{k\times 19}$, and the complete measurement matrix, including the ambiguity states, is constructed using (66) and (67).

D. Fixed integer ambiguity correction

After all measurement corrections have been performed, integer ambiguity resolution is attempted using the LAMBDA algorithm [26]. If an integer vector $\hat{\boldsymbol{N}}_{\text{fixed}}$ sufficiently better than the next best alternative is found, a "pseudo-measurement" correction is performed where $\boldsymbol{N}_{dd}$ is assumed measured with no uncertainty, such that $\mathbf{R}_{\hat{\boldsymbol{N}}_{\text{fixed}}} = \mathbf{0}$. With the simple measurement matrix $\mathbf{H} = [\mathbf{0}_{(k-1)\times 19} \quad \mathbf{I}_{(k-1)\times(k-1)}]$, the fixed state vector is

$$\hat{\boldsymbol{x}}_{\text{fixed}} = \hat{\boldsymbol{x}} + \mathbf{K}(\hat{\boldsymbol{N}}_{\text{fixed}} - \mathbf{H}\hat{\boldsymbol{x}}). \tag{78}$$

Note that because it is not desired to feed the fixed integers back in the MEKF, due to the potentially destabilizing effect it can have, the fixed estimates $\hat{\boldsymbol{x}}_{\text{fixed}}$ are propagated using the expressions in section V-B.2 in parallel with $\hat{\boldsymbol{x}}$ until the next time measurements corrections (and integer ambiguity resolution) are performed, in order to get a high rate "fixed" output.

E. Initialization and handling changes in usable satellites

Position, velocity, clock offsets and clock drift rates are initialized using single-epoch least-squares GNSS estimates. Starting on the ground before launch, roll and pitch are initialized using accelerometer leveling [16],

$$\hat{\phi} = \text{atan2}(-\boldsymbol{f}^b_{\text{IMU},y}, -\boldsymbol{f}^b_{\text{IMU},z}), \tag{79}$$

$$\hat{\theta} = \text{atan2}(\boldsymbol{f}^b_{\text{IMU},x}, \sqrt{(\boldsymbol{f}^b_{\text{IMU},y})^2 + (\boldsymbol{f}^b_{\text{IMU},z})^2}), \tag{80}$$

and heading using a magnetometer. Following this the double differenced ambiguity estimates are initialized using the attitude estimate,

$$\widehat{\nabla\Delta\rho}_{\beta f,s_1s_2} = (\boldsymbol{l}^e_{s_1} - \boldsymbol{l}^e_{s_2})^\top \hat{\mathbf{R}}^e_b \boldsymbol{b}^b, \tag{81}$$

$$\widehat{\nabla\Delta N}_{\beta f,s_1s_2} = \frac{1}{\lambda}\widehat{\nabla\Delta\rho}_{\beta f,s_1s_2} - \nabla\Delta\phi_{\beta f,s_1s_2}. \tag{82}$$

This method is also used to initialize ambiguities whenever a satellite, which was not usable the previous epoch, is to be used, both the first time it is observed and after any signal tracking issues such as cycle slips. Double differenced pseudoranges can also be used for initialization, but for very short baselines the noise present in the pseudoranges can make this undesirable. Gyro biases are initialized by utilizing the known $\boldsymbol{\omega}^b_{eb} = \mathbf{0}$ on the ground before launch, and accelerometer biases are initialized by using the initial attitude, calculated gravity vector and known $\boldsymbol{a}^b_{eb} = \mathbf{0}$.

VII. Experimental testing

The UAV used for data collection was the ET-Air Cruiser Mini, equipped with a Sensonor STIM300 IMU (engineering sample), running at 250Hz output rate, and and two longitudinally spaced antennas connected to U-Blox NEO-M8T receivers. The flight path of the UAV is shown in Fig. 3. All measurements were received by the *SenTiBoard* (sensor timing board) [27], which also receives synchronization signals from each sensor. Using the known delay characteristics of the IMU measurement output [28], the time-of-validity (TOV) output signal and a pulse-per-second (PPS) output of one of the GPS receivers, which signals at the top of each GPST second, the fractional time of validity of the IMU measurements in GPST can be found accurately. This is illustrated in Fig. 4. Combining this with the GNSS measurement timestamps and the estimated clock errors, the absolute time of validity of the IMU measurements can be found. This was used to apply the GNSS measurement corrections with a timing error less than one IMU sample interval (4ms). The difference in measurement time of the GNSS receivers was taken into account in the DDCP measurement, but was not considered for the time of validity of the other measurements, as this difference is smaller than the time between IMU samples.

The MEKF was implemented in Matlab, running on a desktop computer for offline processing. The Matlab implementation of the LAMBDA algorithm from [22] was used for integer ambiguity resolution, using the ratio test with $\mu = 0.5$ to accept integer results. The detection of half cycle errors and cycle slips done by the receivers, and output as flags together with the raw measurements, was used to exclude unusable satellites for the DDCP correction.

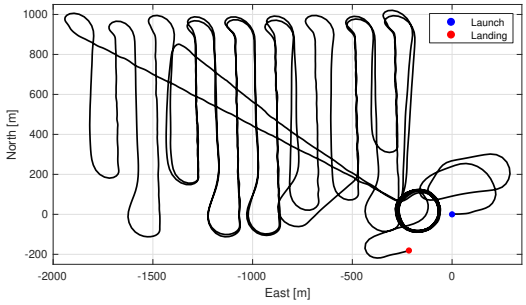

Fig. 3: North-East plot of the flight path.

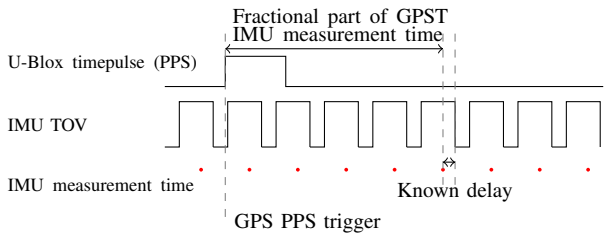

Fig. 4: Time syncronization using the SenTiBoard.

A stationary GNSS receiver was placed near the launch site, logging raw GPS observables. The raw data from the base station and each antenna on the UAV was used for PPK positioning of each antenna using RTKLIB [12]. In addition, RTKLIB was run in "moving base" mode using only the onboard receivers. The estimates using the base station were less noisy, but did not always have the carrier phase integer ambiguities resolved. The moving base results were stiched into these parts of the output. These results were only used for comparison with the results from the MEKF. While the PPK positions are very precise, the accuracy depends on how well the location of the base station is known. Here the position of the base station was assumed to be the average of the "single" position calculated using pseudoranges. Unlike with the implemented algorithm, both GPS, GLONASS and European Geostationary Navigation Overlay System (EGNOS) corrections were used in RTKLIB to calculate the reference signals for comparison.

A. Body frame definition and IMU calibration

When working with vehicle attitude estimation a choice which must be made is how the body frame $\{b\}$ should be defined. One possibility is to use the IMU measurement frame $\{m\}$ as the definition. The calibration matrices $\mathbf{S}_g$ and $\mathbf{S}_f$ would then not include rotation, only scale factor and axis non-orthogonality corrections. The GNSS receiver antenna positions would then need to be known in this frame, which can be difficult if the exact orientation of the IMU in the UAV fuselage is uncertain. Online estimation of the antenna lever arms would then be a possibility. Another option is to define the body frame by the antenna positions themselves, and treat $\{m\}$ and $\{b\}$ as different frames with the same origin.

In this case the vehicle body frame was defined as having its origin at the location of the IMU, x-axis along the baseline between antennas (from back antenna to front), y-axis towards the starboard wing and z-axis downwards giving a right-handed coordinate frame. This allows the simple computation of pitch and heading from antenna positions by using the four-quadrant inverse tangent function. This does however leave the roll-component of the body frame uncertain, in the absence of a third antenna. A separate "alignment" mode was implemented in the MEKF, where the 18 values of the IMU calibration matrices $\mathbf{S}_g$ and $\mathbf{S}_g$ used in (18) and (22) were estimated online. In order to make these observable, the roll estimates from the autopilot, a Pixhawk 2, were used as measurements in the MEKF. For the testing of the MEKF the roll measurement and calibration values in the state vector were removed. The roll measurement used to enable observability of the matrices is of course an error source in itself, which would not be necessary if a third GNSS antenna had been used.

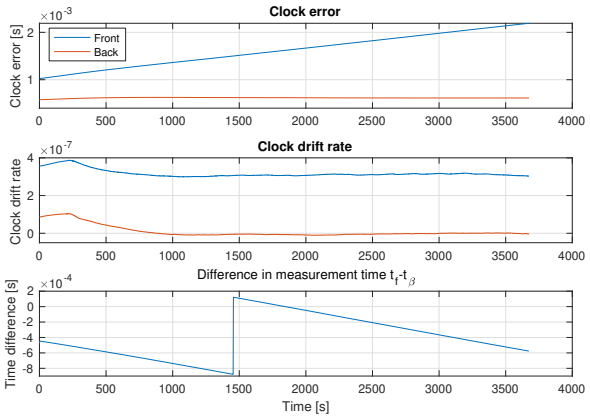

Fig. 5: Estimates of the clock errors and the difference in measurement time between receivers, $t_f - t_\beta$. The jump at around 1450 seconds is caused by the front receiver changing its local measurement time by 1ms.

VIII. Results

Five different measurement configurations were tested:

1) Front antenna only, pseudorange and Doppler.
2) Both antennas, pseudorange, Doppler and DDCP:
   a) No time correction.
   b) Time correction handling satellite movement only, omitting UAV velocities in the correction term of (69).
   c) Time correction using measured Doppler shift, and a simpler measurement model replacing the estimated Doppler shift in (69) with the measurement.
   d) Time correction using the complete model (69).

The estimated clock errors and receiver measurement time difference are plotted in Fig. 5. The estimated mean and RMS errors when compared to PPK (except the roll error, which is compared to the flight controller estimate) are shown in Tab. I. The attitude errors are also plotted in Fig. 6. The differences in position, velocity, roll and pitch results are only minor. Case 2a, with no measurement time correction, is able to resolve integer ambiguities only 18.9% of the time, including many false fixes resulting in a large heading error. This is to be expected from Fig. 2, noting that the estimated float ambiguities do not correspond well to integers if the difference in measurement time is ignored. For case 2b, integer ambiguity resolution failed with a rate of 4.908×10^{-4} and for 2c and 2d only 1.088×10^{-6}. Cases 2c and 2d give nearly identical results, with mean and RMS differences of 1.80×10^{-5}° and 1.64×10^{-4}° respectively, suggesting that the more detailed measurement model may not be worthwhile.

TABLE I: MEKF estimation errors.

Mean	1	2a	2b	2c	2d
$\boldsymbol{p}_x^n$	0.150m	0.187m	0.188m	0.188m	0.188m
$\boldsymbol{p}_y^n$	1.530m	1.478m	1.482m	1.482m	1.482m
$\boldsymbol{p}_z^n$	0.856m	1.067m	1.068m	1.065m	1.065m
$\boldsymbol{v}_x^n$	1.104 $\frac{\text{mm}}{\text{s}}$	0.217 $\frac{\text{mm}}{\text{s}}$	-1.315 $\frac{\text{mm}}{\text{s}}$	-1.104 $\frac{\text{mm}}{\text{s}}$	-1.124 $\frac{\text{mm}}{\text{s}}$
$\boldsymbol{v}_y^n$	-0.597 $\frac{\text{mm}}{\text{s}}$	-0.627 $\frac{\text{mm}}{\text{s}}$	-0.967 $\frac{\text{mm}}{\text{s}}$	-0.579 $\frac{\text{mm}}{\text{s}}$	-0.570 $\frac{\text{mm}}{\text{s}}$
$\boldsymbol{v}_z^n$	0.155 $\frac{\text{mm}}{\text{s}}$	1.114 $\frac{\text{mm}}{\text{s}}$	1.228 $\frac{\text{mm}}{\text{s}}$	0.673 $\frac{\text{mm}}{\text{s}}$	0.656 $\frac{\text{mm}}{\text{s}}$
Roll	0.129°	0.156°	0.159°	0.160°	0.160°
Pitch	0.524°	0.542°	0.529°	0.519°	0.519°
Heading	0.563°	0.757°	0.102°	0.099°	0.099°
RMS					
$\boldsymbol{p}_x^n$	0.356m	0.336m	0.337m	0.337m	0.337m
$\boldsymbol{p}_y^n$	1.548m	1.494m	1.497m	1.498m	1.498m
$\boldsymbol{p}_z^n$	1.843m	1.834m	1.837m	1.838m	1.838m
$\boldsymbol{v}_x^n$	9.936 $\frac{\text{cm}}{\text{s}}$	9.998 $\frac{\text{cm}}{\text{s}}$	9.850 $\frac{\text{cm}}{\text{s}}$	9.838 $\frac{\text{cm}}{\text{s}}$	9.838 $\frac{\text{cm}}{\text{s}}$
$\boldsymbol{v}_y^n$	4.095 $\frac{\text{cm}}{\text{s}}$	4.087 $\frac{\text{cm}}{\text{s}}$	3.980 $\frac{\text{cm}}{\text{s}}$	3.946 $\frac{\text{cm}}{\text{s}}$	3.946 $\frac{\text{cm}}{\text{s}}$
$\boldsymbol{v}_z^n$	8.354 $\frac{\text{cm}}{\text{s}}$	8.137 $\frac{\text{cm}}{\text{s}}$	8.138 $\frac{\text{cm}}{\text{s}}$	8.144 $\frac{\text{cm}}{\text{s}}$	8.143 $\frac{\text{cm}}{\text{s}}$
Roll	0.898°	0.903°	0.902°	0.902°	0.902°
Pitch	1.318°	1.322°	1.310°	1.308°	1.308°
Heading	0.731°	2.150°	0.372°	0.381°	0.381°

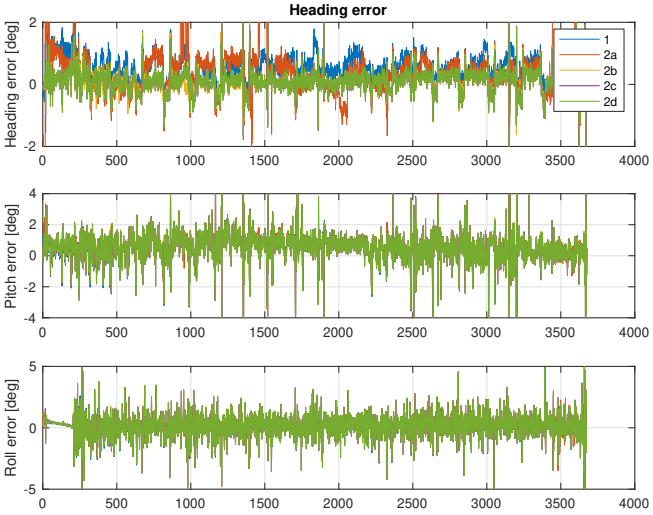

Fig. 6: Attitude error plotted as Euler angles

IX. Conclusion

The results show that use of carrier phase interferometry using low cost receivers can improve the heading estimate compared to the use of a single receiver, and that handling the difference in measurement time is necessary to reliably resolve the integer ambiguities. However, the proposed measurement model yields estimates which are almost identical to those resulting from handling the measurement times using measured Doppler shift, despite increased complexity. Estimates of roll, pitch, position and velocity are almost identical is all the tested cases. An extension left for the future is to add a third receiver, making attitude completely observable, allowing IMU errors to be estimated more accurately. The use of a higher IMU sample rate to reduce integration errors and improve IMU-GNSS timing should also improve the estimates.

References

[1] PX4 Dev team, "Autopilot Hardware - Pixhawk series," 2019. [Online]. Available: https://docs.px4.io/en/flight_controller/pixhawk_series.html

[2] R. E. Kalman, "A New Approach to Linear Filtering and Prediction Problems," *Journal of Basic Engineering*, vol. 82, no. 1, p. 35, 1960.

[3] K. Gade, "The Seven Ways to Find Heading," *Journal of Navigation*, vol. 69, no. 05, pp. 955–970, 2016.

[4] Vectornav, "VN-300," 2019. [Online]. Available: https://www.vectornav.com/purchase/product/vn-300

[5] X. Ji, C. Yu, W. Chen, and D. Dong, "GNSS 3D Attitude Measurement System Based on Dual-Antenna Receiver with Common Clock," in *CPGPC 2017 Forum on Cooperative Positioning and Service*, Harbin, China, 2017, pp. 223–227.

[6] G. Emel'yantsev, E. Dranitsyna, A. Stepanov, B. Blazhnov, and I. Vinokurov, "Tightly-Coupled GNSS-Aided Inertial System with Modulation Rotation of Two-Antenna Measurement Unit," in *2017 DGON Inertial Sensors and Systems (ISS)*. Karlsruhe, Germany: IEEE, 2017.

[7] G. I. Emel'yantsev, A. P. Stepanov, B. A. Blazhnov, D. A. Radchenko, I. Y. Vinokurov, and P. Y. Petrov, "Using satellite receivers with a common clock in a small-sized GNSS compass," *2017 24th Saint Petersburg International Conference on Integrated Navigation Systems, ICINS 2017 - Proceedings*, vol. 116, no. 73, 2017.

[8] G. Emel'yantsev, A. Stepanov, E. Dranitsyna, B. Blazhnov, D. Radchenko, I. Vinokurov, D. Eliseev, and P. Petrov, "DUAL-MODE GNSS GYROCOMPASS USING PRIMARY SATELLITE MEASUREMENTS," in *ICINS 2018*. St. Petersburg, Russia: IEEE, 2018.

[9] Q. Yang, K. Wang, S. H. Li, Y. Liu, and Q. W. Fu, "A Low-cost Attitude Determination Algorithm Based on MEMS IMU dual-antenna GNSS Receiver for UAVs," in *ICINS 2018*. St. Petersburg, Russia: IEEE, 2018.

[10] N. Vasilyuk, M. Vorobiev, and D. Tokarev, "Heading and attitude determination system with low-cost IMU embedded inside one of multiple antennas," pp. 267–274, 2018.

[11] U-Blox, "U-Blox wesite," 2019. [Online]. Available: https://www.u-blox.com/en

[12] T. Takasu, "RTKLIB ver.2.4.3 demo5 b29," 2017. [Online]. Available: http://www.rtklib.com/rtklib.htm

[13] J. G. Garcia, P. I. Mercader, and C. H. Muravchik, "Use of Carrier Phase Double Differences," *Latin American Applied Research*, vol. 35, p. 6, 2005.

[14] P. Henkel and M. Iafrancesco, "Tightly coupled position and attitude determination with two low-cost GNSS receivers," *2014 11th International Symposium on Wireless Communications Systems, ISWCS 2014 - Proceedings*, no. 2, pp. 895–900, 2014.

[15] F. L. Markley, "Attitude Error Representations for Kalman Filtering," *Journal of Guidance, Control, and Dynamics*, vol. 26, no. 2, pp. 311–317, 2003.

[16] P. D. Groves, *Principles of GNSS, Inertial, and Multisensor Integrated Navigation Systems*, 2nd ed., 2013.

[17] P. Misra and P. Enge, *Global Positioning System: Signals, Measurements, and Performance Revised Second Edition*. Ganga-Jamuna Press, 2012.

[18] C. O'Driscoll, "GNSS Solutions," *Inside GNSS*, no. July/August, pp. 18–22, 2010.

[19] E. D. Kaplan and C. J. Hegarty, *Understanding GPS: Principles and applications*, 2nd ed. Norwood, MA, USA: Artech House, 2006.

[20] U-blox, "u-blox 8 / u-blox M8 Receiver Description Including Protocol Specification," 2019. [Online]. Available: https://www.u-blox.com/sites/default/files/products/documents/u-blox8-M8_ReceiverDescrProtSpec_%28UBX-13003221%29_Public.pdf

[21] J. Solà, "Quaternion kinematics for the error-state Kalman filter," 2017. [Online]. Available: http://arxiv.org/abs/1711.02508

[22] S. Verhagen, B. Li, and P. Teunissen, "LAMBDA - Matlab implementation, version 3.0," 2012. [Online]. Available: https://www.researchgate.net/publication/236213370_LAMBDA_software_package_Matlab_implementation_Version_30

[23] C. F. Van Loan, "Computing Integrals Involving the Matrix Exponential," *IEEE Transactions on Automatic Control*, vol. 23, no. 3, pp. 395–404, 1978.

[24] GPS Directorate, "GPS Interface Specification IRN-IS-200H-003," 2015.

[25] J. A. Klobuchar, "Ionospheric Time-Delay Algorithm for Single-Frequency GPS Users," *IEEE Transactions on Aerospace and Electronic Systems*, vol. AES-23, no. 3, pp. 325–331, 1987.

[26] P. J. G. Teunissen, "Least-Squares Estimation of the Integer GPS Ambiguities," in *Invited Lecture for Section IV "Theory and Method-*

ology" at the General Meeting of the International Association of Geodesy, no. August, Beijing, China, 1993, p. 16.

[27] S. M. Albrektsen and T. A. Johansen, "User-Configurable Timing and Navigation for UAVs," *Sensors*, vol. 18, no. 8, 2018.

[28] Sensonor, "Datasheet STIM300 Inertia Measurement Unit TS1524 rev.22," 2018.